

1 **Microbial strong organic ligand production is tightly coupled to iron in**  
2 **hydrothermal plumes**

3  
4 Colleen L. Hoffman<sup>1,2,3\*†</sup> and Patrick J. Monreal<sup>3,4\*†</sup>, Justine B. Albers<sup>5</sup>, Alastair J.M. Lough<sup>6</sup>, Alyson E.  
5 Santoro<sup>5</sup>, Travis Mellett<sup>3,7</sup>, Kristen N. Buck<sup>7,8</sup>, Alessandro Tagliabue<sup>9</sup>, Maeve C. Lohan<sup>6</sup>, Joseph A.  
6 Resing<sup>1,2,3</sup>, Randelle M. Bundy<sup>3</sup>

7  
8 <sup>1</sup>Joint Institute for the Study of Atmosphere and Ocean, University of Washington, 3737 Brooklyn  
9 Avenue NE, Seattle, WA 98195, USA

10 <sup>2</sup>Cooperative Institute for Climate, Ocean, and Ecosystem Studies, University of Washington,  
11 3737 Brooklyn Avenue NE, Seattle, WA 98195, USA

12 <sup>3</sup>School of Oceanography, University of Washington, 1501 NE Boat Street, Seattle, WA 98195,  
13 USA

14 <sup>4</sup>Earth Systems Program, Stanford University, 473 Via Ortega, Stanford, CA 94305,  
15 USA

16 <sup>5</sup>Department of Ecology, Evolution, and Marine Biology, University of California, Santa Barbara,  
17 CA 93106, USA

18 <sup>6</sup>Department of Ocean and Earth Sciences, National Oceanography Centre, University of  
19 Southampton, European Way, Southampton SO14 3ZH, United Kingdom

20 <sup>7</sup>College of Marine Science, University of South Florida, 140 7<sup>th</sup> Avenue South, St. Petersburg,  
21 FL, 33701, USA

22 <sup>8</sup>College of Earth, Oceans, and Atmospheric Sciences, Oregon State University, 2651 SW Orchard Ave,  
23 Corvallis, OR, 97331, USA

24 <sup>9</sup>Department of Earth, Ocean, and Ecological Sciences, University of Liverpool, 4 Brownlow  
25 Street, Liverpool l69 3GP, United Kingdom

26  
27 †These authors contributed equally and are co-first authors

28 \*Correspondence: Colleen L. Hoffman and Patrick J. Monreal

29 **Email:** [clhoffma@gmail.com](mailto:clhoffma@gmail.com), [pmonreal@uw.edu](mailto:pmonreal@uw.edu)

30

31

32

33

34 **Abstract.** Hydrothermal vents have emerged as important sources of iron to seawater, yet only a subset of  
35 this iron is soluble and persists long enough to impact the deep ocean iron inventory. The longevity and  
36 solubility of iron in seawater is in part governed by strong organic ligands, like siderophores, that are  
37 produced by microorganisms and are a part of the ocean's dissolved organic iron-binding ligand pool. These  
38 ligands have been hypothesized to aid in the persistence of dissolved iron in hydrothermal environments. To  
39 explore this hypothesis, we measured iron and iron-binding ligands including siderophores from 11  
40 geochemically distinct sites along a 1,700 km section of the Mid-Atlantic Ridge. Siderophores were found  
41 in hydrothermal plumes at all sites, with proximity to the vent playing an important role in dictating  
42 siderophore type and diversity. The notable presence of amphiphilic siderophores may point to microbial  
43 utilization of siderophores to access particulate hydrothermal iron, and the exchange of dissolved and  
44 particulate iron. The tight coupling between strong ligands and dissolved iron within neutrally buoyant  
45 plumes across distinct hydrothermal environments, and the presence of dissolved siderophores with  
46 siderophore-producing microbial genera, suggests that biological production of ligands influence iron  
47 chemistry in hydrothermal systems.

## 48 **1. Introduction**

49 Over the last few decades, observations and modelling efforts have increased our understanding about the  
50 critical role organic ligands play in the cycling, transport, and utilization of trace metals (Tagliabue et al.,  
51 2017; Buck et al., 2018; Bundy et al., 2018; Moore et al., 2021; Hawkes et al., 2013b; Kleint et al., 2016).  
52 Iron (Fe) binding organic ligands in seawater have a wide range of sources, which are only just beginning to  
53 be understood. Recent observations suggest that microbial production of siderophores, humic-like substances  
54 and exopolysaccharides are some of the major contributors of marine organic ligands (Hassler et al., 2017),  
55 and microbial production and alteration of ligands influences Fe cycling in environments ranging from  
56 hydrothermal plumes (Cowen and Bruland, 1985; Cowen et al., 1990) to the open ocean (Lauderdale et al.,  
57 2020; Whitby et al., 2024, 2020; Misumi et al., 2013). Strong Fe-binding organic ligands (defined as L<sub>1</sub>  
58 ligands) are a heterogeneous mixture of microbially produced compounds that are operationally classified  
59 based on their binding strength with Fe (defined as  $\log K_{Fe',FeL}^{cond} > 12$ ). They are thermodynamically favored  
60 to complex and stabilize external sources of Fe to prevent its scavenging and removal (Fishwick et al., 2014;  
61 Aguilar-Islas et al., 2010).

62  
63 Siderophores are the strongest known Fe-binding organic ligands. They are produced by bacteria and fungi  
64 to facilitate Fe uptake and solubilize otherwise inaccessible phases in the marine environment (Butler, 2005;  
65 Manck et al., 2022). They have primarily been considered an important microbial strategy for Fe acquisition  
66 in the low dissolved Fe (dFe) surface ocean (Vraspir and Butler, 2009; Butler, 2005). However, siderophore  
67 uptake and biosynthesis genes were observed in >70% of Fe-related bacterial transcripts in a hydrothermal  
68 environment in Guaymas Basin (Li et al., 2014), have been identified in oxygen-deficient zones (Moore et

69 al., 2021), and are a common Fe acquisition strategy within terrestrial and pathogenic ecosystems (Sandy and  
70 Butler, 2009), all of which are environments where Fe concentrations are orders of magnitude higher than  
71 surface seawater.

72

73 Previous studies have examined unknown Fe-binding ligands in hydrothermal plumes and throughout the  
74 deep ocean (Buck et al., 2018; Kleint et al., 2016; Hawkes et al., 2013b; Sander and Koschinsky, 2011), as  
75 well as siderophores observed below the euphotic zone (Bundy et al., 2018; Park et al., 2023a; Moore et al.,  
76 2021; Boiteau et al., 2019). However, no previous studies have ever directly measured siderophores in  
77 hydrothermal systems due to the high sample volume requirements, difficulty in obtaining deep ocean trace  
78 metal samples, and the time-intensive nature of the analyses. A ‘stabilizing agent’ (i.e. ligands) has been  
79 proposed for the long-range transport of hydrothermal dFe into the ocean interior. The role of strong Fe-  
80 binding ligands in hydrothermal dFe transport represents an important knowledge gap in how hydrothermal  
81 vents may impact the ocean dFe inventory (Resing et al., 2015) and how siderophores may influence Fe  
82 transformations in hydrothermal systems. Here, for the first time, we identified siderophores and siderophore-  
83 producing microbes in 11 geochemically distinct hydrothermal environments along the slow-spreading (20-  
84 50 mm/yr) Mid-Atlantic Ridge (MAR). Four black smokers (high temperature, high Fe), four off-axis sites,  
85 one diffuse vent (low temperature, low Fe), one alkaline vent (pH 9-11, very low Fe), and one non-vent  
86 fracture zone were investigated using both competitive ligand exchange-adsorptive cathodic stripping  
87 voltammetry and state-of-the-art liquid chromatography coupled to electrospray ionization mass  
88 spectroscopy (Boiteau et al., 2016) in a targeted approach to search for known siderophores and possible  
89 compounds present in the L<sub>1</sub> ligand pool in hydrothermal environments. Microbial community analysis was  
90 also compared at three sites to understand whether microbial ligand production impacts Fe transformation in  
91 hydrothermal systems. Overall, our results show microbially-produced siderophores were present in all sites,  
92 and that strong L<sub>1</sub> ligands were tightly coupled to hydrothermal dFe concentrations in neutrally-buoyant  
93 plume samples in this system. The presence of organic ligands produced by bacteria in hydrothermal systems  
94 suggest that they play an important role in deep ocean Fe cycling.

## 95 **2. Results and Discussion**

### 96 **2.1 The role of iron-binding ligands in hydrothermal plumes**

97 Strong Fe-binding ligands (L<sub>1</sub>) have previously been found in neutrally-buoyant hydrothermal plumes across  
98 a variety of systems (Tagliabue et al., 2017; Resing et al., 2015; Buck et al., 2018; Hawkes et al., 2013b;  
99 Wang et al., 2022; Bennett et al., 2008). However, the relationship between organic ligands and dFe have  
100 never been investigated together systematically across a wide variety of vents in the same study. In this work,  
101 the average binding strength and concentration of organic Fe-binding ligands were quantified in 11 vent  
102 systems that spanned a wide range in dFe concentrations (0.41-90 nM) and underlying vent geology. Over  
103 99% of dFe in the neutrally buoyant plume samples were complexed by L<sub>1</sub> ligands and the ligands were  
104 almost always completely saturated with dFe, meaning Fe-free ‘excess’ L<sub>1</sub> ligands capable of binding

105 additional Fe were present in low concentrations ( $< 1$  nM; **Fig. S1**). As a result, dFe concentrations were  
106 tightly coupled to  $L_1$  ligands in a nearly 1:1 ratio (**Fig. 1d**), similar to previous studies in other neutrally  
107 buoyant plumes (**Fig. 1e**) (Lough et al., 2022; Buck et al., 2018, 2015).

108 The strong coupling between dFe and ligands was only observed at sites where  $L_1$  ligands were detected.  
109 Some samples, that were closer to the buoyant plume and vent source, contained high concentrations of  
110 weaker ligands ( $\log K_{Fe,FeL}^{cond} < 12$ , **Table S2-S3**) whose concentrations had no correlation with dFe. This is  
111 consistent with these environments likely being dominated by complex Fe phases, which could include  
112 various inorganic forms (e.g. nanopyrite, Fe-oxyhydroxide) as well as mixed organic phases of Fe as  
113 hydrothermal fluids initially mix with oxygenated seawater. High concentrations of weaker ligands have also  
114 been observed in samples near the vent orifice in previous studies (Hawkes et al., 2013). In this study, we are  
115 not able to discern the exact chemical composition of the ligands we detect via voltammetric methods, and  
116 thus the weaker and some portion of the stronger ligands we observe likely represent a mix of different  
117 inorganic and organic ligands. Similar to what was described in Hawkes et al. (2013), the ligands we measure  
118 could represent multiple layers of coordination bonds, forming complex Fe phases, similar to the “onion”  
119 concept (Mackey and Zirino, 1994). For example, colloidal Fe phases are common in hydrothermal vents  
120 and can form aggregates that bind Fe, but not in traditional organic coordination bonds (Fitzsimmons et al.,  
121 2017; Honeyman and Santschi, 1989). There are also likely processes occurring near the vent source in such  
122 a complex environment that cause some Fe phases to be in various stages of disequilibria that we also measure  
123 as ligands via our voltammetric methods.

124

125 The sources of weaker Fe-binding ligands ( $\log K_{Fe,FeL}^{cond} < 12$ ) that have been observed in other hydrothermal  
126 systems is not well understood, and their impact on Fe cycling over the lifetime of neutrally-buoyant plume  
127 is unclear. Recent studies have shown microbes may use siderophores or siderophore-like (strong binding  
128 ligands) ligands to access Fe associated with weaker ligands — such as humic substances and thiols — to  
129 enhance the bioavailability of Fe (Kuhn et al., 2014; Muller, 2018). However, to date, the few studies that  
130 have explored ligand concentrations and binding strengths within hydrothermal systems (Buck et al., 2015,  
131 2018; Kleint et al., 2016; Hawkes et al., 2013c; Sander and Koschinsky, 2011) have mixed hypotheses as to  
132 the role and sources of weaker-type ligands within plumes. Additional studies are needed to investigate the  
133 sources and mechanisms of weaker-type ligands in hydrothermal plumes and understand their impact on the  
134 Fe cycle in hydrothermal systems.

135

136 In the neutrally buoyant plume samples, stronger  $L_1$  ligands were present and were correlated with the dFe  
137 concentrations (**Fig. 1**) and weaker ligands were no longer dominant. In other systems with a high dFe and  
138 ligand endmember such as estuaries, a decrease in weaker ligands along with dFe concentrations has also  
139 been observed (Buck et al., 2007; Bundy et al., 2014). This has been interpreted as a scavenging of weaker  
140 Fe-ligand complexes, while the dFe that remains in solution is that which is bound to stronger ligands (Bundy  
141 et al., 2014). A similar control on dFe concentrations by  $L_1$  ligands has also been previously observed in

142 aerosol solubility experiments (Fishwick et al., 2014). There are a few possible explanations for the  
143 correlation of dFe and L<sub>1</sub> ligands in the neutrally-buoyant plume. One possible explanation is that both the  
144 dFe and L<sub>1</sub> ligands originate from the vent fluids themselves, yielding a tightly coupled hydrothermal  
145 endmember. However, the concentration of L<sub>1</sub> ligands did not correlate with excess mantle Helium-3 (<sup>3</sup>He<sub>xs</sub>,  
146 **Fig S2, Table S2-S3**) (Lough et al., 2022), a nearly conservative tracer of the mixing of hydrothermal fluids  
147 with seawater (Buck et al., 2018). Moreover, our samples closer to the vent source were dominated by weaker  
148 organic ligands showing no correlation to dFe. This suggests the L<sub>1</sub> ligands were not directly sourced from  
149 the vent fluids along with dFe. Biological sources represent another likely explanation for the coupling of L<sub>1</sub>  
150 ligands and dFe, if the ligands observed in the neutrally-buoyant plume are from bacteria that produced them  
151 in surrounding deep ocean seawater that was then entrained, local production from vent-biota and/or  
152 microbial mats, diffusion from microbial production in sediments, or *in-situ* production by bacteria within  
153 the neutrally buoyant plume (Dick et al., 2013; Li et al., 2014; Sheik et al., 2015; Mellett et al., *submitted.*).

## 154 **2.2 The presence of siderophores in hydrothermal systems**

155 Siderophores were measured in a subset of the samples to further explore the source of the L<sub>1</sub> ligands coupled  
156 to dFe in the neutrally-buoyant plume. Marine organic ligand composition changes with environmental  
157 gradients (Boiteau et al., 2016; Gledhill and Buck, 2012), making the structure and functional groups of  
158 siderophores identified in hydrothermal samples of particular interest. Somewhat surprisingly, siderophores  
159 were found in all samples and we observed a large diversity of siderophores with high confidence using mass-  
160 to-charge ratio (*m/z*), MS/MS spectra, and specific chromatographic characteristics (**Fig. 2a**). On-axis  
161 spreading centers contained the highest dFe concentrations (> 20 nM) and wider variety of siderophores than  
162 samples from fracture zones, diffuse, and off-axis sites (dFe ≤ 1 nM). The greatest number of distinct  
163 siderophores were identified at Lucky Strike, Broken Spur, Rainbow, and TAG (**Fig. 2**). On average, 13  
164 compounds were identified with high confidence per on-axis spreading center sample, compared with 5 per  
165 diffuse/fracture zone sample, and 2.5 per off-axis sample (**Fig. 2b, Fig. S4**). Mixed-type siderophores —  
166 containing different moieties that bind to Fe(III) — were common at all sites. Hydroxamates were identified  
167 at and around spreading centers, yet none of these were detected with high confidence in samples from  
168 diffuse/fracture zones (**Fig. S4**). Summed siderophore abundance in neutrally-buoyant plumes above  
169 spreading centers was similarly more than twice that of samples from fracture zones or off-axis (**Fig. 2c**).  
170 Thus, vent type and proximity played a role in the diversity and abundance of siderophore types observed,  
171 likely related to the diversity of the microbial community and/or unique Fe acquisition strategies across sites.

172  
173 Siderophores are putatively part of the operational L<sub>1</sub> ligand pool based on their binding strength (Gledhill  
174 and Buck, 2012), and patterns in their distributions were similar to those of the strong ligands. The peak areas  
175 of each putative siderophore we identified were used as a proxy for concentrations (*section 3.3*), and these  
176 concentrations significantly correlated with dFe, as observed with dFe and L<sub>1</sub> ligands (**Fig. 2b**). Siderophores  
177 were present in concentrations similar to the surface ocean (Boiteau et al., 2016; Moore et al., 2021; Park et

178 al., 2022; Bundy et al., 2018) and were equivalent to concentrations representing 0.01-0.4% of the total L<sub>1</sub>  
179 ligands (**Table 1**). This is a substantial underestimate of siderophore contributions to the L<sub>1</sub> ligand pool due  
180 to analytical constraints in identifying unknown siderophores. Recent work on siderophore biosynthesis  
181 pathways and advances in genome mining suggest that known siderophores represent a small fraction of what  
182 is expected to be produced in nature (Hider and Kong, 2010; Reitz et al., 2022), and our analyses in this study  
183 were limited to only known siderophores. We also restricted our reporting to compounds identified with very  
184 high confidence (**Fig 2a, S3**). In addition, most siderophores are not commercially available to use as  
185 standards, and individual siderophores have different ionization or extraction efficiencies. The extraction  
186 efficiency for the solid phase extraction technique is approximately 5-10% for bulk Fe-binding organics  
187 (Bundy et al., 2018) and 40% for a siderophore standard (Waska et al., 2015). Employing both corrections  
188 yields siderophore contributions to the total L<sub>1</sub> pool of 0.1-4% and 0.025-1%, respectively. We are inevitably  
189 missing many naturally occurring unknown compounds, and thus we consider this a lower bound. Regardless  
190 of the small percentage contribution to total L<sub>1</sub> ligands, it is evident that microbially produced siderophores  
191 were ubiquitous across all vent sites and had similar distributional patterns as L<sub>1</sub> ligands. There are also likely  
192 other compounds such as some strong binding humics that are also contributing to the L<sub>1</sub> ligand pool (Laglera  
193 and van den Berg, 2009). Future work with much larger water volumes will be able to reduce uncertainty and  
194 identify a greater number of compounds. Still, the identification of siderophores here — and their relationship  
195 with dFe — provides compelling evidence that microbial production of ligands is responsible for at least  
196 some portion of the tight coupling between L<sub>1</sub> and dFe in hydrothermal systems along the MAR.

197

198 The presence and diversity of siderophores identified in this system was surprising given the relatively high  
199 Fe concentrations of hydrothermal environments, but some compelling patterns were observed. For example,  
200 previous work has shown that low Fe surface waters have higher concentrations of amphiphilic siderophores  
201 compared to high Fe coastal waters (Boiteau et al., 2016), and amphiphilic siderophores are less common in  
202 terrestrial environments (Hider and Kong, 2010). Amphiphilic siderophores have long hydrocarbon tails that  
203 can be embedded into the lipid bilayer of the bacterial cell membrane providing a mechanism to shuttle Fe  
204 into the cell and prevent diffusive loss (Martinez et al., 2003). Amphiphilic siderophores comprised 57% of  
205 the siderophores in our samples (**Fig. S5**), supporting the ubiquity of amphiphilic siderophores in marine  
206 environments (Butler and Theisen, 2010). Amphiphilic siderophores were found in concentrations between  
207 0.3-4.7 pM, with the highest concentrations found at Rainbow (**Fig. 2d, Table S6**). These concentrations  
208 were similar to those observed in the upper ocean (Boiteau et al., 2016; Bundy et al., 2018; Boiteau et al.,  
209 2019). Marine bacteria produce suites of amphiphilic siderophores as a way to adapt to the change in  
210 hydrophilicity in the surrounding environment (Sandy and Butler, 2009; Homann et al., 2009). Amphiphilic  
211 siderophores in plumes could be a way for bacteria to access Fe as they are physically transported and cope  
212 with strong chemical gradients, similar to the production of multiple siderophores in terrestrial and  
213 pathogenetic systems as a means to access inorganic particulate Fe for cellular uptake and storage (Hider and  
214 Kong, 2010).

215

### 216 **2.3 Microbial sources of siderophores in hydrothermal plumes**

217 The high diversity of siderophores across a huge range of hydrothermal vent systems revealed several  
218 surprising aspects of Fe cycling. The biosynthesis of a siderophore is energy-intensive and is regulated by Fe  
219 concentration in the surrounding environment (Rizzi et al., 2019). Siderophore presence suggests that bacteria  
220 are producing these compounds despite the overall higher Fe concentrations in the deep ocean and within  
221 hydrothermal plumes. Consistent with siderophore utilization in terrestrial ecosystems (Hider and Kong,  
222 2010; Sandy and Butler, 2009), one hypothesis is that siderophore production is beneficial to bacteria in the  
223 plumes for transforming Fe from otherwise inaccessible forms, such as particulate nanopyrites or Fe  
224 oxyhydroxides that are present close to the vent source. To explore the potential for microbial production of  
225 siderophores, we examined microbial community composition around Rainbow (St. 11, 17) and Lucky Strike  
226 (St. 7; **Table 1, Table S1**) using 16S rRNA gene-based amplicon sequencing to detect bacteria with the  
227 metabolic potential to synthesize siderophores (**Fig. 3, S11**), where the presence of taxa encoding siderophore  
228 biosynthetic gene clusters indicates whether the microbial community is genetically capable of producing the  
229 compounds we observed. Bacterial genera containing known siderophore-producers were found at all three  
230 MAR sites examined, and putative siderophore-producers represented 3-20% of the relative abundance of  
231 the community (**Fig. 3**). Putative siderophore-producers were more abundant in the 3  $\mu\text{m}$  (particle-attached)  
232 size fraction than in the 0.2  $\mu\text{m}$  (free-living) fraction, suggesting siderophore production is more common in  
233 particle-associated bacteria in hydrothermal environments.

234

235 We found microbial genera in our samples that can produce a subset of the siderophores identified here,  
236 including ferrioxamines, vibrioferrin, and acinetoferrin (Butler, 2005; Vraspir and Butler, 2009; Moore et al.,  
237 2021; Bundy et al., 2018; Boiteau et al., 2016). Genera with the genetic potential to produce ferrioxamines  
238 were present at all three sites, while those known to produce vibrioferrin were present at Lucky Strike and  
239 Rainbow, and those producing acinetoferrin were also present at Rainbow (**Table S1, S7**). Mycobactins were  
240 detected with high confidence in every sample of this study, and genes encoding mycobactin have been  
241 detected in a cultured organism from a hydrothermal system (Gu et al., 2019), but no mycobactin producers  
242 were identified in this study. We detected woodybactin D with high confidence in 5 out of 11 sites. Although  
243 these biosynthetic genes were not identified in any of the genera observed, woodybactin D is a carboxylate  
244 siderophore isolated from *Shewanella* (Carmichael et al., 2019), and groups of deep-sea *Shewanella* (Kato  
245 and Nogi, 2001) were found in the dataset (**Fig. S11**). The biosynthesis genes for many of the siderophores  
246 identified are unknown. Thus, finding genera capable of producing only a subset of the siderophores  
247 characterized is not surprising. The observation that a significant portion of the *in-situ* microbial community  
248 is capable of synthesizing siderophores (**Fig 3**) suggests that siderophore production is more widespread in  
249 the deep ocean than previously believed.

250

## 251 **2.4 The impact of strong ligands and siderophores on dissolved iron in neutrally-buoyant plumes**

252 Evidence that siderophores are ubiquitous in the marine environment — including higher Fe environments  
253 — has been increasing (Park et al., 2023b). The high dFe associated with hydrothermal plumes may still not  
254 be high enough to suppress siderophore production due to the elevated Fe requirements of heterotrophic  
255 bacteria (Tortell et al., 1996). It is also likely that not all of the Fe is bio-accessible in hydrothermal plumes.  
256 Soil microbes secrete siderophores to solubilize particulate Fe (Crowley et al., 1991) and similar processes  
257 could be occurring in hydrothermal plumes, where Fe mineral phases associated with organic compounds are  
258 common (Hoffman et al., 2020; Toner et al., 2009; Fitzsimmons et al., 2017; Hoffman et al., 2018; German  
259 and Seyfried, 2014; Holden et al., 2012). Although our measurements suggest that dFe in the neutrally-  
260 buoyant plume is likely dominated by organic complexation, the L<sub>1</sub> measurements alone cannot distinguish  
261 between purely organic phases or a mixture of inorganic and organic ligands in complex aggregations or  
262 small colloids, as discussed above (*section 2.1*). Given the evidence from particulate Fe studies in neutrally-  
263 buoyant plumes (Hoffman et al., 2020; Toner et al., 2009; Yücel et al., 2011; Fitzsimmons et al., 2014, 2017;  
264 Hoffman et al., 2018), it is highly likely that some portion of what is detected in the L<sub>1</sub> pool is a mixture of  
265 organic and inorganic Fe in small colloids which are operationally in the dFe pool (Fitzsimmons et al., 2017).  
266 It is also telling that most siderophore-producing genera were found to be particle-associated (**Fig. 3**),  
267 providing additional evidence that siderophores might be produced to solubilize particulate Fe or access other  
268 colloidal phases. Further work that assesses why bacteria are producing siderophores in neutrally buoyant  
269 plumes will be important for understanding microbial metabolism in these systems, and the impact of  
270 siderophore production on Fe dispersal.

271

272 Organic Fe-binding ligands have been implicated in playing a critical role in the preservation and transport  
273 of hydrothermal dFe into the ocean interior (Hoffman et al., 2018; Resing et al., 2015; Fitzsimmons et al.,  
274 2017; Toner et al., 2009; Bennett et al., 2011, 2008; Buck et al., 2018; Sander and Koschinsky, 2011). In this  
275 work, L<sub>1</sub> ligands were tightly coupled to dFe in neutrally buoyant plumes along the MAR and the presence  
276 of siderophores in these samples provided evidence for the first time, that at least some of these ligands are  
277 microbially produced. How these complexes may facilitate the exchange of Fe between dissolved and  
278 particulate phases (Fitzsimmons et al., 2017), and whether siderophores are present across additional  
279 hydrothermal vent systems will aid in constraining the biogeochemical importance of microbial feedbacks in  
280 impacting the hydrothermal dFe supply to the deep ocean.

281

## 282 **3. Appendix: Materials and Methods**

### 283 **3.1 Sampling and cruise transect**

284 Samples were collected as part of the 2017-2018 U.K. GEOTRACES GA13 section cruise along the Mid-  
285 Atlantic Ridge. Water samples from 11 venting and near venting locations were collected using a Seabird  
286 911 conductivity, temperature, and depth (CTD) titanium rosette using conducting Kevlar wire with an



287 oxidation-reduction potential (ORP) sensor to detect plumes. Teflon coated OTE (Ocean Test Equipment)  
288 bottles were pressurized to approximately 7 psi with 0.2  $\mu\text{m}$  filtered air using an oil free compressor. A  
289 Sartobran 300 (Sartorius) filter capsule (0.2  $\mu\text{m}$ ) was used to collect filtered seawater samples into clean 250  
290 mL LDPE sample bottles. Bottles and caps were rinsed 3 times with the filtered sample before being filled.  
291 Samples were stored frozen at  $-20^{\circ}\text{C}$  for Fe-organic ligand characterization by voltammetry and mass  
292 spectrometry.

### 293 **3.2 Fe-binding ligand concentration and binding strengths Competitive Ligand Exchange-Adsorptive** 294 **Cathodic Stripping Voltammetry**

295 Fe-binding ligand concentrations and binding strengths (defined as conditional binding constants,  $\log K_{\text{Fe}, \text{FeL}}^{\text{cond}}$   
296  $> 12$ ) were determined by competitive ligand exchange-adsorptive cathodic stripping voltammetry (CLE-  
297 ACSV) with a BASi controlled growth mercury electrode (CGME) with an Ag/AgCl<sup>-</sup> reference electrode  
298 and platinum auxiliary electrode (Bioanalytical Systems Incorporated). Using previously established  
299 methods (Buck et al., 2015, 2018; Bundy et al., 2018; Abualhaija and van den Berg, 2014; Hawkes et al.,  
300 2013c), 40 frozen filtrate ( $<0.2 \mu\text{m}$ ) samples with dFe concentrations between 0.41-11.67 nM (**Table S1-**  
301 **S2**) were thawed in a  $4^{\circ}\text{C}$  fridge prior to analysis. A 15-point titration curve was analyzed for each sample.  
302 Briefly, within each titration, every point sequentially received 10 mL of sample, 7.5 mM of borate-  
303 ammonium buffer, 10  $\mu\text{M}$  salicylaldehyde (SA) added ligand, and a dFe addition. Samples were then  
304 equilibrated overnight before being measured on the BASi. Data was collected using the *Epsilon Eclipse*  
305 *Electrochemical Analyzer* (v.213) with a deposition time of 120 seconds and analyzed using *ElectroChemical*  
306 *Data Software* (v2001-2014) and *PromCC* (v2008-2018) to determine peak areas and Fe-binding ligand  
307 parameters, respectively. All results were confirmed to fall within the analytical window of the method by  
308 comparing the side reaction coefficient of the added ligand  $\alpha_{\text{SA}}$  to the side reaction coefficient of the natural  
309 ligands detected ( $\alpha_{\text{L}}$ ). If the  $\alpha_{\text{L}}$  was within an order of magnitude of  $\alpha_{\text{SA}}$  then the results were deemed to fall  
310 within the analytical window.

### 311 **3.3 Reverse Titration-CLE-ACSV**

312 Reverse titration-CLE-ACSV (RT-CLE-ACSV) (Hawkes et al., 2013a) was completed on 10 samples from  
313 Broken Spur, and TAG hydrothermal vent fields with dFe concentrations between 19.01-90.25 nM (**Table**  
314 **S3**). Briefly, a 10-point titration curve was analyzed for each sample with each titration point consisting of  
315 10 mL of sample buffered with 7.5 mM boric acid and the competitive ligand 1-nitroso-2-naphthol (NN)  
316 additions. All samples were analyzed on a BASi Controlled Growth Mercury Electrode (CGME) with the  
317 *Epsilon Eclipse Electrochemical Analyzer* (v.213) and deposition time of 120 seconds. For each sample,  
318 competitive ligand NN additions were 0.5, 1, 2, 3, 4, 6, 9, 15, 20, and 40  $\mu\text{M}$ . Samples were equilibrated  
319 overnight and purged with  $\text{N}_2$  (99.99%) for 5 minutes before analysis. At the end of each titration, three Fe  
320 additions (3-15 nM) were added to the final titration point to get the total concentration of Fe in equilibrium  
321 with ligands. Data was analyzed using *ElectroChemical Data Software* (v2001-2014) to acquire peak areas

322 and a package in R using the model parameters of  $\beta_{\text{FeNN3}} = 5.12 \times 10^{16}$ ,  $\chi_{\text{min}} = 0.8$ ,  $\chi_{\text{max}} = 0.9$ , and  $c_{\text{high}} =$   
323 0.75 to determine the Fe-binding ligand parameters (Hawkes et al., 2013a). These parameters were chosen  
324 based on the recommendations for undersaturated samples and titrations curves where  $i_{p_{\text{max}}}$  was not reached  
325 (Hawkes et al., 2013a). All other parameters within the model we kept at the default values.

### 326 **3.4 Siderophore quantification and characterization**

327 In addition to measuring Fe-binding ligands by voltammetry, we also identified and quantified siderophores.  
328 Between 0.65-1.5 L of 0.2  $\mu\text{m}$  filtered seawater pooled from ligand samples at each site (described above)  
329 was pumped slowly (15-20  $\text{mL min}^{-1}$ ) onto a polystyrene-divinylbenzene (Bond Elut ENV) solid phase  
330 extraction (SPE) column (Bundy et al., 2018; Boiteau et al., 2016). SPE columns were rinsed with MilliQ  
331 and stored at  $-20^{\circ}\text{C}$  until analysis. For the analytical measurements, samples were thawed in the dark, eluted  
332 in 12 mL of distilled methanol, and dried down to between 0.2-0.5 mL of sample eluent (**Table S1**). Aliquots  
333 were analyzed by reverse-phase liquid chromatography (LC) on a trace metal clean bio-inert LC (Thermo  
334 Dionex 3000 NCS). The LC was interfaced with an electrospray ionization-mass spectrometer (ESI-MS;  
335 Thermo Q-Exactive HF) to identify and quantify the compounds based on accurate mass ( $\text{MS}^1$ ) and the  
336 fragmentation ( $\text{MS}^2$ ) data (Bundy et al., 2018; Boiteau et al., 2016). MSconvert (Proteowizard) was used to  
337 convert MS data to an open source mzxML format, and two stages of data processing were conducted using  
338 modified versions of previously reported R scripts (Bundy et al., 2018; Boiteau et al., 2016). In the first stage,  
339 mzxML files were read into R using new package “RaMS” (Kumler and Ingalls, 2022), and extracted ion  
340 chromatograms (EICs) were generated for each targeted  $m/z$  of interest from an in-house database of  
341 siderophores. The  $m/z$  targets were the ionized apo,  $^{54}\text{Fe}$ -bound, and  $^{56}\text{Fe}$ -bound version of each siderophore,  
342 with a tolerance of 7.5 ppm. Putative siderophore candidates were filtered through a series of hard thresholds,  
343 such that  $\text{MS}^1$  spectra were quality controlled to contain a minimum of 25 datapoints and the maximum  
344 intensity of each EIC was greater than 1e4 counts. Spectra meeting these criteria and containing either  $^{54}\text{Fe}$ -  
345 bound and  $^{56}\text{Fe}$ -bound  $m/z$  peaks within 30 seconds of each other or an apo peak were displayed for the user  
346 to further inspect peak quality and make the final decision of whether to move on to stage two of processing  
347 with a given siderophore candidate.

348

349 Stage two of processing extracted  $\text{MS}^2$  spectra of the apo and Fe-bound forms of candidate siderophores to  
350 compare with the predicted  $\text{MS}^2$  generated by *in silico* fragmenter MetFrag (Ruttkies et al., 2016). The *in*  
351 *silico* fragmenter feature was run with a tolerance of 10 ppm on “[M+H] $^{+}$ ” and “[M+Na] $^{+}$ ” modes. A  
352 confidence level of 1-4, from highest to lowest confidence, was then assigned to putative siderophores based  
353 on the following criteria: (1) peaks were present in  $\text{MS}^1$  and  $\text{MS}^2$  spectra, and at least one of the three most-  
354 intense  $\text{MS}^2$  fragments matched *in silico* fragmentation, (2) peaks were present in  $\text{MS}^1$  and  $\text{MS}^2$  spectra, and  
355 smaller-intensity fragments matched *in silico* fragmentation, (3) peaks were present in  $\text{MS}^1$  and  $\text{MS}^2$  spectra,  
356 but little to no fragments matched *in silico* fragmentation, and (4) nicely shaped peaks were identified in  $\text{MS}^1$   
357 spectra but no  $\text{MS}^2$  spectra was collected (outlined in **Table S5**; example spectra in **Fig. S6-S9**). The

358 confidence levels were modelled after reporting standards for metabolite identification (Sumner et al., 2007).  
359 MetFrag pulls chemical structures from publicly-available databases like PubChem or COCONUT (Sorokina  
360 et al., 2021), which contain most, but not all variations of siderophores. As such, Fe-bound candidates were  
361 usually run against the apo form available in the database, and for siderophores with similar structures but  
362 variations in fatty chain length or double bond placement, sometimes only one parent structure was available.

363  
364 A 5-point standard curve with known concentrations of siderophore ferrioxamine E was used for  
365 quantification of putative siderophores, with a limit of detection of 0.257 nM in the eluent (**Fig. S10**), or  
366 0.07-0.21 pM in the sample depending on sample-to-eluent volume ratio at each site (**Table S1**). MS<sup>1</sup> peaks  
367 were integrated for all putatively identified siderophores and peak areas were converted to concentration  
368 using the standard curve and the concentration factor of sample volume to eluent volume (**Fig. S10**).  
369 Commercial standards are not available for most siderophores, and different compounds have distinct  
370 ionization efficiencies in ESI-MS. Thus, the siderophore concentrations reported here are estimates of  
371 siderophore concentrations in these environments based on ferrioxamine E, chosen for its commercial  
372 availability and use in prior studies (e.g., (Boiteau et al., 2016)). Additionally, 1 mM of cyanocobalamin was  
373 added as an internal standard to each sample aliquot to address any changes in sensitivity during LC-ESI-MS  
374 runs. All putative siderophores that were identified with peak areas less than the detection limit were  
375 discarded, and all remaining putative compounds with at least confidence levels 1 and 2 at one site were  
376 included in the manuscript and are referred to as siderophores throughout. Siderophore identifications remain  
377 putative due to inherent uncertainty with assignments by mass, but the confidence levels were designed such  
378 that high confidence candidates contain siderophore-like moieties in their fragments. Limited sample  
379 volumes prevented analysis via LC-ICP-MS like previous studies, which, in addition to greater availability  
380 of commercial standards and more analytical comparisons between ferrioxamine E with other siderophore  
381 types, would allow definitive characterization in future studies. Confidence level 3 and 4 putative  
382 siderophores are only included in the Supplementary Information (**Table S6**). In a final step of quality  
383 control, EICs for <sup>13</sup>C isotopologues of candidates were inspected to verify matching peak structure.

### 384 **3.5 Microbial community analysis**

385 Microbial community composition was assessed in neutrally buoyant plumes and near venting sites at three  
386 sites: Lucky Strike (Station 7; 1670 m), 10 km S of Rainbow (Station 17; 2000 m), and 200 km E of Rainbow  
387 (Station 11; 600 m, 1600 m and 2250 m). A range of 1- 2 L of seawater were filtered by pressure filtration  
388 through sequential 25 mm membrane filters housed in polypropylene filter holders (Whatman SwinLok, GE  
389 Healthcare, Pittsburgh, Pennsylvania) using a peristaltic pump and silicone tubing. Samples first passed  
390 through a 3 µm pore-size polyester membrane filter (Sterlitech, Auburn, Washington) then onto a 0.2 µm  
391 pore-size polyethersulfone membrane filter (Supor-200, Pall Corporation, Port Washington, New York).  
392 Pump tubing was acid washed with 10% hydrochloric acid and flushed with ultrapure water between each

393 sample. The filters were flash frozen in liquid nitrogen in 2 mL gasketed bead beating tubes (Fisher Scientific)  
394 at sea.

395

396 Nucleic acids (DNA) were extracted as described previously (Santoro et al., 2010), with slight modifications.  
397 Briefly, cells on the filters were lysed directly in the bead beating tubes with sucrose-ethylene diamine  
398 tetraacetic acid (EDTA) lysis buffer (0.75 M sucrose, 20 mM EDTA, 400 mM NaCl, 50 mM Tris) and 1%  
399 sodium dodecyl sulfate. Tubes were then agitated in a bead beating machine (Biospec Products) for 1 min,  
400 and subsequently heated for 2 min. at 99°C in a heat block. Proteinase K (New England Biolabs) was added  
401 to a final concentration of 0.5 mg/mL. Filters were incubated at 55°C for approximately 4 h and the resulting  
402 lysates were purified with the DNeasy kit (Qiagen) using a slightly modified protocol (Santoro et al., 2010).  
403 The purified nucleic acids were eluted in 200 µL of DNase, RNase-free water, and quantified using a  
404 fluorometer (Qubit and Quanti-T HS reagent, Invitrogen Molecular Probes).

405

406 The 16S rRNA gene was amplified in all samples using V4 primers (Apprill et al., 2015; Parada et al., 2016)  
407 (515F-Y and 806RB) following a previously established protocol (Stephens et al., 2020). Amplicons were  
408 sequenced using a paired-end 250bp run on an Illumina MiSeq 500 and demultiplexed by the UC Davis  
409 Genome Center. The resulting 16S rRNA amplicon sequences were filtered and trimmed using the DADA2  
410 pipeline in R (Callahan et al., 2016). Taxonomic assignments were made with version 138.1 of the SILVA  
411 SSU database (Quast et al., 2013) (silva\_nr99\_v138.1\_wSpecies\_train\_set.fa.gz ;  
412 doi:10.5281/zenodo.4587955; accessed March 2022). Chloroplast and mitochondrial sequences were filtered  
413 out of the dataset using the 'phyloseq' R package (v 1.38.0), after which samples had read depths ranging  
414 from 9375 – 65486 reads (average 28425 ± 20014 reads) and represented 1010 unique amplicon sequence  
415 variants (ASVs). Read counts were transformed from absolute to relative abundance and taxa were  
416 aggregated to the Family level. The ten most abundant families present in each sample were visualized using  
417 the 'ggplot2' package (v. 3.3.5).

418

419 In order to assess the potential of the observed prokaryotic taxa to produce siderophores, we downloaded all  
420 siderophore biosynthetic gene clusters (BGCs) in the antimash secondary metabolite database ( $n = 7909$ )  
421 and used text-string matching to compare genera containing these BGCs to the genera found in our 16S rRNA  
422 gene dataset (Blin et al., 2021). We cross-referenced the nomenclature of antimash-predicted siderophores  
423 with that of the siderophores identified by LC-ESI-MS in this study, accounting for minor differences in  
424 naming convention between the two databases, to determine if microbial community members present at  
425 each site were predicted to make any of the siderophores that were measured at that site. Station 38 and  
426 Station 12 were the closest sites with siderophore measurements for comparison against the taxonomic  
427 samples taken at 200 km E of Rainbow and 10 km S of Rainbow, respectively. Samples for microbial  
428 taxonomy and siderophore identity were taken from the same location at Lucky Strike and thus directly  
429 compared.

430

431 **Data Availability**

432 The CSV data reported in this study has been deposited at Zenodo under the DOI:  
433 <http://doi.org/10.5281/zenodo.7325154>. The LC-ES-MS data has been deposited on Massive under the DOI:  
434 <http://doi.org/doi.10.25345/C5V97ZW7N>. Microbial 16S rRNA data have been deposited on GenBank under  
435 the accession number BioProject #PRJNA865382. All data is freely available on each of these data  
436 repositories.

437

438

439 **Acknowledgments**

440 We acknowledge the captain and crew of the R/V *James Cook*, Chief Scientist Alessandro Tagliabue, and  
441 Noah Gluschkoff for supporting this work. This study was a part of the FeRidge project (GEOTRACES  
442 section GA13) which was supported by the Natural Environment Research Council funding (NERC United  
443 Kingdom Grants NE/N010396/1 to MCL and NE/N009525/1 to AT). The International GEOTRACES  
444 Programme is possible in part thanks to the support from the U.S. National Science Foundation (Grant OCE-  
445 1840868) to the Scientific Committee on Oceanic Research (SCOR). CLH was funded by JISAO/CICOES  
446 postdoctoral fellowship. PJM was funded through the NOAA Hollings Scholar summer program. JR was  
447 funded by NOAA Ocean Exploration and Research, NOAA Earth-Ocean Interactions programs at NOAA-  
448 Pacific Marine Environmental Lab (PMEL #5955), and UW-CICOES (CICOES #2024-1385). Part of this  
449 work was carried out in the University of Washington TraceLab, which receives support from the M.J.  
450 Murdock Charitable Trust in conjunction with the University of Washington College of Environment, and  
451 the Pacific Marine Environmental Labs at the National Oceanic and Atmospheric Administration. Parts of  
452 this work was also carried out in Dr. Anitra Ingalls laboratory with the help of Laura Truxal and Dr. Jiwoon  
453 Park at the University of Washington-School of Oceanography.

454

455 **Author Contributions:** Manuscript preparation, sample/data processing, CSV analysis, and interpretation  
456 LC-ESI-MS data analysis and interpretation (C.L.H. and P.J.M.), microbial analysis and interpretation  
457 (J.B.A. and A.E.S.), dissolved iron and derived excess  $^3\text{He}_{xs}$  measurements, sample collection (A.J.M. L. and  
458 M.C.L.), microbial data collection and ligand data interpretation (T.M. and K.N.B.), and project design and  
459 planning, data interpretation, and mentoring (A.T., M.C.L., J.A.R., and R.M.B.). All authors were involved  
460 in editing and revision of the manuscript.

461

462 **Competing Interest Statement:** The authors declare no competing interests.

463

464 **References**

465 Abualhija, M. M. and van den Berg, C. M. G. G.: Chemical speciation of iron in seawater using catalytic

466 cathodic stripping voltammetry with ligand competition against salicylaldoxime, *Mar. Chem.*, 164, 60–74,  
467 <https://doi.org/10.1016/j.marchem.2014.06.005>, 2014.

468 Aguilar-Islas, A. M., Wu, J., Rember, R., Johansen, A. M., and Shank, L. M.: Dissolution of aerosol-derived  
469 iron in seawater: Leach solution chemistry, aerosol type, and colloidal iron fraction, *Mar. Chem.*, 120, 25–  
470 33, 2010.

471 Apprill, A., McNally, S., Parsons, R., and Weber, L.: Minor revision to V4 region SSU rRNA 806R gene  
472 primer greatly increases detection of SAR11 bacterioplankton, *Aquat. Microb. Ecol.*, 75, 129–137,  
473 <https://doi.org/10.3354/ame01753>, 2015.

474 Bazylev, B. A.: Allochemical Metamorphism of Mantle Peridotites in the Hayes Fracture Zone of the North  
475 Atlantic, *Petrology*, 5, 362–379, 1997.

476 Beaulieu, S. E. and Szafranski, K. M.: InterRidge Global Database of Active Submarine Hydrothermal Vent  
477 Fields Version 3.4, <https://doi.org/10.1594/PANGAEA.917894>, 2020.

478 Bennett, S. a., Achterberg, E. P., Connelly, D. P., Statham, P. J., Fones, G. R., and German, C. R.: The  
479 distribution and stabilisation of dissolved Fe in deep-sea hydrothermal plumes, *Earth Planet. Sci. Lett.*, 270,  
480 157–167, <https://doi.org/10.1016/j.epsl.2008.01.048>, 2008.

481 Bennett, S. a., Hansman, R. L., Sessions, A. L., Nakamura, K. ichi, and Edwards, K. J.: Tracing iron-fueled  
482 microbial carbon production within the hydrothermal plume at the Loihi seamount, *Geochim. Cosmochim.*  
483 *Acta*, 75, 5526–5539, <https://doi.org/10.1016/j.gca.2011.06.039>, 2011.

484 Blin, K., Shaw, S., Kautsar, S. A., Medema, M. H., and Weber, T.: The antiSMASH database version 3:  
485 Increased taxonomic coverage and new query features for modular enzymes, *Nucleic Acids Res.*, 49, D639–  
486 D643, <https://doi.org/10.1093/nar/gkaa978>, 2021.

487 Boiteau, R. M., Mende, D. R., Hawco, N. J., McIlvin, M. R., Fitzsimmons, J. N., Saito, M. A., Sedwick, P.  
488 N., DeLong, E. F., and Repeta, D. J.: Siderophore-based microbial adaptations to iron scarcity across the  
489 eastern Pacific Ocean, *Proc. Natl. Acad. Sci.*, 113, 14237–14242, <https://doi.org/10.1073/pnas.1608594113>,  
490 2016.

491 Boiteau, R. M., Till, C. P., Coale, T. H., Fitzsimmons, J. N., Bruland, K. W., and Repeta, D. J.: Patterns of  
492 iron and siderophore distributions across the California Current System, *Limnol. Oceanogr.*, 64, 376–389,  
493 <https://doi.org/10.1002/lno.11046>, 2019.

494 Buck, K. N., Sohst, B., and Sedwick, P. N.: The organic complexation of dissolved iron along the U.S.  
495 GEOTRACES (GA03) North Atlantic Section, *Deep. Res. Part II Top. Stud. Oceanogr.*, 116, 152–165,  
496 <https://doi.org/10.1016/j.dsr2.2014.11.016>, 2015.

497 Buck, K. N., Sedwick, P. N., Sohst, B., and Carlson, C. A.: Organic complexation of iron in the eastern  
498 tropical South Pacific: Results from US GEOTRACES Eastern Pacific Zonal Transect (GEOTRACES cruise  
499 GP16), *Mar. Chem.*, 201, 229–241, <https://doi.org/10.1016/j.marchem.2017.11.007>, 2018.

500 Bundy, R. M., Boiteau, R. M., McLean, C., Turk-Kubo, K. A., McIlvin, M. R., Saito, M. A., Mooy, B. A.  
501 Van, and Repeta, D. J.: Distinct Siderophores Contribute to Iron Cycling in the Mesopelagic at Station  
502 ALOHA, *Front. Mar. Sci.*, 1–15, <https://doi.org/10.3389/fmars.2018.00061>, 2018.

503 Butler, A.: Marine siderophores and microbial iron mobilization., *Biometals*, 18, 369–374,  
504 <https://doi.org/10.1007/s10534-005-3711-0>, 2005.

505 Butler, A. and Theisen, R. M.: Iron(III)-siderophore coordination chemistry: Reactivity of marine  
506 siderophores., *Coord. Chem. Rev.*, 254, 288–296, <https://doi.org/10.1016/j.ccr.2009.09.010>, 2010.

507 Callahan, B. J., McMurdie, P. J., Rosen, M. J., Han, A. W., Johnson, A. J. A., and Holmes, S. P.: DADA2:  
508 High-resolution sample inference from Illumina amplicon data, *Nat. Methods*, 13, 581–583,

509 <https://doi.org/10.1038/nmeth.3869>, 2016.

510 Carmichael, J. R., Zhou, H., and Butler, A.: A suite of asymmetric citrate siderophores isolated from a marine  
511 *Shewanella* species, *J. Inorg. Biochem.*, 198, 1–6, <https://doi.org/10.1016/j.jinorgbio.2019.110736>, 2019.

512 Cowen, J. P. and Bruland, K. W.: Metal deposits associated with bacteria: implications for Fe and Mn marine  
513 biogeochemistry, *Deep Sea Res. Part A. Oceanogr. Res. Pap.*, 32, 253–272, [https://doi.org/10.1016/0198-0149\(85\)90078-0](https://doi.org/10.1016/0198-0149(85)90078-0), 1985.

515 Cowen, J. P., Massoth, G. J., and Feely, R. A.: Scavenging rates of dissolved manganese in a hydrothermal  
516 vent plume, *Deep Sea Res. Part A. Oceanogr. Res. Pap.*, 37, 1619–1637, [https://doi.org/10.1016/0198-0149\(90\)90065-4](https://doi.org/10.1016/0198-0149(90)90065-4), 1990.

518 Crowley, D. E., Wang, Y. C., Reid, C. P. P., and Szaniszlo, P. J.: Mechanisms of iron acquisition from  
519 siderophores by microorganisms and plants, *Plant Soil*, 130, 179–198, 1991.

520 Dick, G. J., Anantharaman, K., Baker, B. J., Li, M., Reed, D. C., and Sheik, C. S.: The microbiology of deep-  
521 sea hydrothermal vent plumes: ecological and biogeographic linkages to seafloor and water column habitats.,  
522 *Front. Microbiol.*, 4, 124, <https://doi.org/10.3389/fmicb.2013.00124>, 2013.

523 Fishwick, M. P., Sedwick, P. N., Lohan, M. C., Worsfold, P. J., Buck, K. N., Church, T. M., and Ussher, S.  
524 J.: The impact of changing surface ocean conditions on the dissolution of aerosol iron, *Global Biogeochem.*  
525 *Cycles*, 28, 1235–1250, <https://doi.org/10.1002/2014GB004921>, 2014.

526 Fitzsimmons, J. N., Boyle, E. a., and Jenkins, W. J.: Distal transport of dissolved hydrothermal iron in the  
527 deep South Pacific Ocean, *Proc. Natl. Acad. Sci.*, 111, 16654–16661,  
528 <https://doi.org/10.1073/pnas.1418778111>, 2014.

529 Fitzsimmons, J. N., John, S. G., Marsay, C. M., Hoffman, C. L., Nicholas, S. L., Toner, B. M., German, C.  
530 R., and Sherrell, R. M.: Iron persistence in the distal hydrothermal plume supported by dissolved – particulate  
531 exchange, *Nat. Geosci.*, 10, 1–8, <https://doi.org/10.1038/ngeo2900>, 2017.

532 German, C. and Seyfried, W. E.: *Hydrothermal Processes*, 2nd ed., Elsevier Ltd., 1–39 pp.,  
533 <https://doi.org/10.1016/B978-0-08-095975-7.00201-1>, 2014.

534 Gledhill, M. and Buck, K. N.: The organic complexation of iron in the marine environment: A review, *Front.*  
535 *Microbiol.*, 3, 1–17, <https://doi.org/10.3389/fmicb.2012.00069>, 2012.

536 Gu, H., Sun, Q., Luo, J., Zhang, J., and Sun, L.: A First Study of the Virulence Potential of a *Bacillus subtilis*  
537 Isolate From Deep-Sea Hydrothermal Vent, *Front. Cell. Infect. Microbiol.*, 9, 1–14,  
538 <https://doi.org/10.3389/fcimb.2019.00183>, 2019.

539 Hassler, C. S., van den Berg, C. M. G., and Boyd, P. W.: Toward a regional classification to provide a more  
540 inclusive examination of the ocean biogeochemistry of iron-binding ligands, *Front. Mar. Sci.*, 4,  
541 <https://doi.org/10.3389/fmars.2017.00019>, 2017.

542 Hawkes, J. A., Gledhill, M., Connelly, D. P., and Achterberg, E. P.: Characterisation of iron binding ligands  
543 in seawater by reverse titration, *Anal. Chim. Acta*, 766, 53–60, <https://doi.org/10.1016/j.aca.2012.12.048>,  
544 2013a.

545 Hawkes, J. A., Connelly, D. P., Gledhill, M., and Achterberg, E. P.: The stabilisation and transportation of  
546 dissolved iron from high temperature hydrothermal vent systems, *Earth Planet. Sci. Lett.*, 375, 280–290,  
547 <https://doi.org/10.1016/j.epsl.2013.05.047>, 2013b.

548 Hawkes, J. A., Connelly, D. P., Gledhill, M., and Achterberg, E. P.: The stabilisation and transportation of  
549 dissolved iron from high temperature hydrothermal vent systems, *Earth Planet. Sci. Lett.*, 375, 280–290,  
550 <https://doi.org/10.1016/j.epsl.2013.05.047>, 2013c.

- 551 Hider, R. C. and Kong, X.: Chemistry and biology of siderophores, *Nat. Prod. Rep.*, 27, 637–657,  
552 <https://doi.org/10.1039/b906679a>, 2010.
- 553 Hoffman, C. L., Nicholas, S. L., Ohnemus, D. C., Fitzsimmons, J. N., Sherrell, R. M., German, C. R., Heller,  
554 M. I., Lee, J. mi, Lam, P. J., and Toner, B. M.: Near-field iron and carbon chemistry of non-buoyant  
555 hydrothermal plume particles, Southern East Pacific Rise 15°S, *Mar. Chem.*, 201, 183–197,  
556 <https://doi.org/10.1016/j.marchem.2018.01.011>, 2018.
- 557 Hoffman, C. L., Schladweiler, C., Seaton, N. C. A., Nicholas, S. L., Fitzsimmons, J., Sherrell, R. M., German,  
558 C. R., Lam, P., and Toner, B. M.: Diagnostic morphology and solid-state chemical speciation of  
559 hydrothermally derived particulate Fe in a long-range dispersing plume, *ACS Earth Sp. Chem.*, 4, 1831–  
560 1842, <https://doi.org/10.1021/acsearthspacechem.0c00067>, 2020.
- 561 Holden, J., Breier, J., Rogers, K., Schulte, M., and Toner, B.: Biogeochemical processes at hydrothermal  
562 vents: microbes and minerals, bioenergetics, and carbon fluxes, *Oceanography*, 25, 196–208,  
563 <https://doi.org/http://dx.doi.org/10.5670/oceanog.2012.18>, 2012.
- 564 Homann, V. V., Sandy, M., Tincu, J. A., Templeton, A. S., Tebo, B. M., and Butler, A.: Loihichelins A - F ,  
565 a Suite of Amphiphilic Siderophores Produced by the Marine Bacterium Halomonas LOB-5, *J. Nat. Prod.*,  
566 72, 884–888, 2009.
- 567 Honeyman, B. D. and Santschi, P. H.: A Brownian-pumping model for oceanic trace metal scavenging:  
568 evidence from Th isotopes, 1989.
- 569 Kato, C. and Nogi, Y.: Correlation between phylogenetic structure and function : examples from deep-sea  
570 *Shewanella*, 35, 223–230, 2001.
- 571 Kelley, D. S. and Shank, T. M.: Hydrothermal systems: A decade of discovery in slow spreading  
572 environments, *Geophys. Monogr. Ser.*, 188, 369–407, <https://doi.org/10.1029/2010GM000945>, 2010.
- 573 Kleint, C., Hawkes, J. A., Sander, S. G., and Koschinsky, A.: Voltammetric Investigation of Hydrothermal  
574 Iron Speciation, *Front. Mar. Sci.*, 3, 1–11, <https://doi.org/10.3389/fmars.2016.00075>, 2016.
- 575 Kuhn, K. M., Maurice, P. A., States, U., Neubauer, E., Hofmann, T., and Kammer, F. Von Der: Accessibility  
576 of Humic-Associated Fe to a Microbial Siderophore: Implications for Bioavailability, *Environ. Sci. Technol.*,  
577 1015–1022, 2014.
- 578 Kumler, W. and Ingalls, A. E.: The R Journal: Tidy Data Neatly Resolves Mass-Spectrometry’s Ragged  
579 Arrays, *R J.*, 2022.
- 580 Laglera, L. M. and van den Berg, C. M. G.: Evidence for geochemical control of iron by humic substances  
581 in seawater, *Limnol. Oceanogr.*, 54, 610–619, 2009.
- 582 Lauderdale, J. M., Braakman, R., Forget, G., Dutkiewicz, S., and Follows, M. J.: Microbial feedbacks  
583 optimize ocean iron availability, *Proc. Natl. Acad. Sci. U. S. A.*, 117, 4842–4849,  
584 <https://doi.org/10.1073/pnas.1917277117>, 2020.
- 585 Li, M., Toner, B. M., Baker, B. J., Breier, J. a, Sheik, C. S., and Dick, G. J.: Microbial iron uptake as a  
586 mechanism for dispersing iron from deep-sea hydrothermal vents., *Nat. Commun.*, 5, 3192,  
587 <https://doi.org/10.1038/ncomms4192>, 2014.
- 588 Lough, A. J. M., Tagliabue, A., Demasy, C., Resing, J. A., Mellett, T., Wyatt, N. J., and Lohan, M. C.: The  
589 impact of hydrothermal vent geochemistry on the addition of iron to the deep ocean, *Biogeosciences Discuss.*,  
590 [preprint], 1–23, <https://doi.org/10.5194/bg-2022-73>, 2022.
- 591 Mackey, D. J. and Zirino, A.: Comments on trace metal speciation in seawater or do “onions” grow in the  
592 sea?, *Anal. Chim. Acta*, 284, 635–647, 1994.



593 Manck, L. E., Park, J., Tully, B. J., Poire, A. M., Bundy, R. M., Dupont, C. L., and Barbeau, K. A.:  
594 Petrobactin, a siderophore produced by *Alteromonas*, mediates community iron acquisition in the global  
595 ocean, *ISME J.*, 16, 358–369, <https://doi.org/10.1038/s41396-021-01065-y>, 2022.

596 Martinez, J. S., Carter-Franklin, J. N., Mann, E. L., Martin, J. D., Haygood, M. G., and Butler, A.: Structure  
597 and membrane affinity of a suite of amphiphilic siderophores produced by a marine bacterium, *Proc. Natl.*  
598 *Acad. Sci. U. S. A.*, 100, 3754–3759, <https://doi.org/10.1073/pnas.0637444100>, 2003.

599 Mellett, T., Albers, J. B., Santoro, A., Wang, W., Salaun, P., Resing, J., Lough, A. J. ., Tagliabue, A., Lohan,  
600 M., Bundy, R. M., and Buck, K. N.: Particle exchange mediated by organic ligands in incubation experiments  
601 of hydrothermal vent plumes along the mid-Atlantic Ridge, n.d.

602 Misumi, K., Lindsay, K., Moore, J. K., Doney, S. C., Tsumune, D., and Yoshida, Y.: Humic substances may  
603 control dissolved iron distributions in the global ocean: Implications from numerical simulations, *Global*  
604 *Biogeochem. Cycles*, 27, 450–462, 2013.

605 Moore, L. E., Heller, M. I., Barbeau, K. A., Moffett, J. W., and Bundy, R. M.: Organic complexation of iron  
606 by strong ligands and siderophores in the eastern tropical North Pacific oxygen deficient zone, *Mar. Chem.*,  
607 236, 104021, <https://doi.org/10.1016/j.marchem.2021.104021>, 2021.

608 Muller, F. L. L.: Exploring the Potential Role of Terrestrially Derived Humic Substances in the Marine  
609 Biogeochemistry of Iron, *Front. Earth Sci.*, 6, 1–20, <https://doi.org/10.3389/feart.2018.00159>, 2018.

610 Omanović, D., Garnier, C., and Pižeta, I.: ProMCC: An all-in-one tool for trace metal complexation studies,  
611 *Mar. Chem.*, 173, 25–39, <https://doi.org/10.1016/j.marchem.2014.10.011>, 2015.

612 Parada, A. E., Needham, D. M., and Fuhrman, J. A.: Every base matters: Assessing small subunit rRNA  
613 primers for marine microbiomes with mock communities, time series and global field samples, *Environ.*  
614 *Microbiol.*, 18, 1403–1414, <https://doi.org/10.1111/1462-2920.13023>, 2016.

615 Park, J., Durham, B. P., Key, R. S., Groussman, R. D., Pinedo-Gonzalez, P., Hawco, N. J., John, S. G.,  
616 Carlson, M. C. G., Lindell, D., Juranek, L., Ferrón, S., Ribalet, F., Armbrust, E. V., Ingalls, A. E., and Bundy,  
617 R. M.: Siderophore production and utilization by microbes in the North Pacific Ocean, *bioRxiv*,  
618 2022.02.26.482025, <https://doi.org/10.1101/2022.02.26.482025>, 2022.

619 Park, J., Durham, B. P., Key, R. S., Groussman, R. D., Bartolek, Z., Pinedo-Gonzalez, P., Hawco, N. J., John,  
620 S. G., Carlson, M. C. G., and Lindell, D.: Siderophore production and utilization by marine bacteria in the  
621 North Pacific Ocean, *Limnol. Oceanogr.*, 68, 1636–1653, 2023a.

622 Park, J., Durham, B. P., Key, R. S., Groussman, R. D., Pinedo-Gonzalez, P., Hawco, N. J., John, S. G.,  
623 Carlson, M. C. G., Lindell, D., Juranek, L., Ferrón, S., Ribalet, F., Armbrust, E. V., Ingalls, A. E., and Bundy,  
624 R. M.: Siderophore production and utilization by microbes in the North Pacific Ocean, *Limnol. Oceanogr.*,  
625 2022.02.26.482025, <https://doi.org/10.1002/lno.12373>, 2023b.

626 Quast, C., Pruesse, E., Yilmaz, P., Gerken, J., Schweer, T., Yarza, P., Peplies, J., and Glöckner, F. O.: The  
627 SILVA ribosomal RNA gene database project: Improved data processing and web-based tools, *Nucleic Acids*  
628 *Res.*, 41, 590–596, <https://doi.org/10.1093/nar/gks1219>, 2013.

629 Reitz, Z. L., Butler, A., and Medema, M. H.: Automated genome mining predicts combinatorial diversity and  
630 taxonomic distribution of peptide metallophore structures, *bioRxiv*, 15–20,  
631 <https://doi.org/https://doi.org/10.1101/2022.12.14.519525>, 2022.

632 Resing, J. a., Sedwick, P. N., German, C. R., Jenkins, W. J., Moffett, J. W., Sohst, B. M., and Tagliabue, A.:  
633 Basin-scale transport of hydrothermal dissolved metals across the South Pacific Ocean, *Nature*, 523, 200–  
634 203, <https://doi.org/10.1038/nature14577>, 2015.

635 Rizzi, A., Roy, S., Bellenger, J. P., and Beauregard, P. B.: Iron homeostasis in *Bacillus subtilis* requires  
636 siderophore production and biofilm formation, *Appl. Environ. Microbiol.*, 85,

637 <https://doi.org/10.1128/AEM.02439-18>, 2019.

638 Ruttkies, C., Schymanski, E. L., Wolf, S., Hollender, J., and Neumann, S.: MetFrag relaunched: incorporating  
639 strategies beyond in silico fragmentation, *J. Cheminform.*, 8, 1–16, [https://doi.org/10.1186/s13321-016-](https://doi.org/10.1186/s13321-016-0115-9)  
640 0115-9, 2016.

641 Sander, S. G. and Koschinsky, A.: Metal flux from hydrothermal vents increased by organic complexation,  
642 *Nat. Geosci.*, 4, 145–150, <https://doi.org/10.1038/ngeo1088>, 2011.

643 Sandy, M. and Butler, A.: Microbial iron acquisition: marine and terrestrial siderophores., *Chem. Rev.*, 109,  
644 4580–95, <https://doi.org/10.1021/cr9002787>, 2009.

645 Santoro, A. E., Casciotti, K. L., and Francis, C. A.: Activity, abundance and diversity of nitrifying archaea  
646 and bacteria in the central California Current, *Environ. Microbiol.*, 12, 1989–2006,  
647 <https://doi.org/10.1111/j.1462-2920.2010.02205.x>, 2010.

648 Sheik, C. S., Anantharaman, K., Breier, J. A., Sylvan, J. B., Edwards, K. J., and Dick, G. J.: Spatially resolved  
649 sampling reveals dynamic microbial communities in rising hydrothermal plumes across a back-arc basin.,  
650 *ISME J.*, 9, 1434–45, <https://doi.org/10.1038/ismej.2014.228>, 2015.

651 Sorokina, M., Merseburger, P., Rajan, K., Yirik, M. A., and Steinbeck, C.: COCONUT online: Collection of  
652 Open Natural Products database, *J. Cheminform.*, 13, 1–13, <https://doi.org/10.1186/s13321-020-00478-9>,  
653 2021.

654 Stephens, B. M., Opalk, K., Petras, D., Liu, S., Comstock, J., Aluwihare, L. I., Hansell, D. A., and Carlson,  
655 C. A.: Organic Matter Composition at Ocean Station Papa Affects Its Bioavailability, Bacterioplankton  
656 Growth Efficiency and the Responding Taxa, *Front. Mar. Sci.*, 7, <https://doi.org/10.3389/fmars.2020.590273>,  
657 2020.

658 Sumner, L. W., Amberg, A., Barrett, D., Beale, M. H., Beger, R., Daykin, C. A., Fan, T. W.-M., Fiehn, O.,  
659 Goodacre, R., Griffin, J. L., Hankemeier, T., Hardy, N., Harnly, J., Higashi, R., Kopka, J., Lane, A. N.,  
660 Lindon, J. C., Marriott, P., Nicholls, A. W., Reily, M. D., Thaden, J. J., and Viant, M. R.: Proposed minimum  
661 reporting standards for chemical analysis, *Metabolomics*, 3, 211–221, [https://doi.org/10.1007/s11306-007-](https://doi.org/10.1007/s11306-007-0082-2)  
662 0082-2, 2007.

663 Tagliabue, A., Bowie, A. R., Boyd, P. W., Buck, K. N., Johnson, K. S., and Saito, M. A.: The integral role  
664 of iron in ocean biogeochemistry, *Nature*, 543, 51–59, <https://doi.org/10.1038/nature21058>, 2017.

665 Toner, B. M., Fakra, S. C., Manganini, S. J., Santelli, C. M., Marcus, M. a., Moffett, J. W., Rouxel, O.,  
666 German, C. R., and Edwards, K. J.: Preservation of iron(II) by carbon-rich matrices in a hydrothermal plume,  
667 *Nat. Geosci.*, 2, 197–201, <https://doi.org/10.1038/ngeo433>, 2009.

668 Tortell, P. D., Maldonado, M. T., and Price, N. M.: The role of heterotrophic bacteria in iron-limited ocean  
669 ecosystems, *Nature*, 383, 330–332, <https://doi.org/10.1038/383330a0>, 1996.

670 Vraspir, J. M. and Butler, A.: Chemistry of marine ligands and siderophores., *Ann. Rev. Mar. Sci.*, 1, 43–63,  
671 <https://doi.org/10.1146/annurev.marine.010908.163712>, 2009.

672 Wang, H., Wang, W., Liu, M., Zhou, H., Ellwood, M. J., Butterfield, D. A., Buck, N. J., and Resing, J. A.:  
673 Iron ligands and isotopes in hydrothermal plumes over backarc volcanoes in the Northeast Lau Basin,  
674 Southwest Pacific Ocean, *Geochim. Cosmochim. Acta*, 336, 341–352, 2022.

675 Waska, H., Koschinsky, A., Ruiz Chanco, M. J., and Dittmar, T.: Investigating the potential of solid-phase  
676 extraction and Fourier-transform ion cyclotron resonance mass spectrometry (FT-ICR-MS) for the isolation  
677 and identification of dissolved metal-organic complexes from natural waters, *Mar. Chem.*, 173, 78–92,  
678 <https://doi.org/10.1016/j.marchem.2014.10.001>, 2015.

679 Whitby, H., Planquette, H., Cassar, N., Bucciarelli, E., Osburn, C. L., Janssen, D. J., Cullen, J. T., González,

680 A. G., Völker, C., and Sarthou, G.: A call for refining the role of humic-like substances in the oceanic iron cycle, *Sci. Rep.*, 10, 6144, 2020.

682 Whitby, H., Park, J., Shaked, Y., Boiteau, R. M., Buck, K. N., and Bundy, R. M.: New insights into the  
683 organic complexation of bioactive trace metals in the global ocean from the GEOTRACES era,  
684 *Oceanography*, 37, 142–155, 2024.

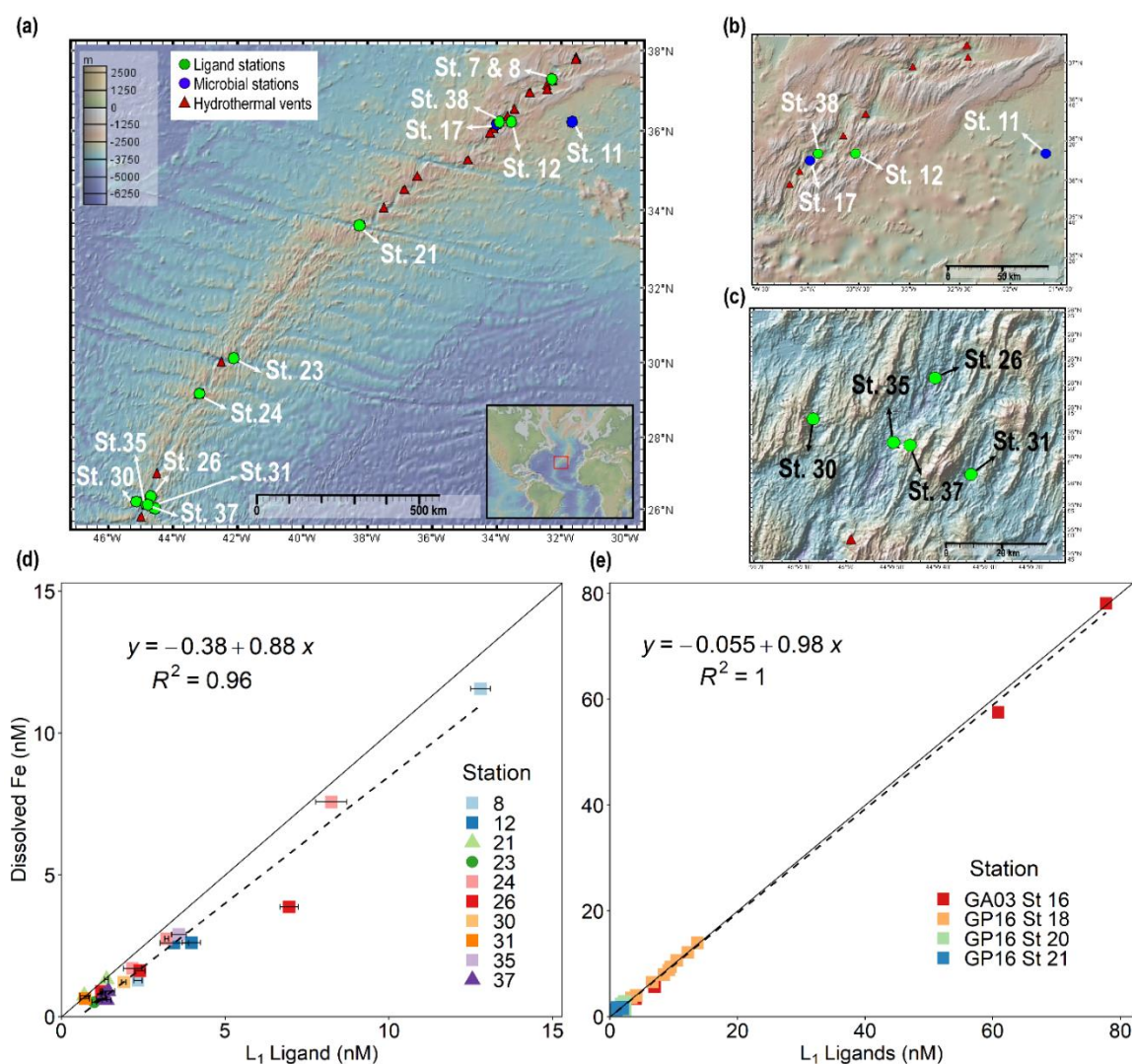
685 Yücel, M., Gartman, A., Chan, C. S., and Luther, G. W.: Hydrothermal vents as a kinetically stable source  
686 of iron-sulphide-bearing nanoparticles to the ocean, *Nat. Geosci.*, 4, 367–371,  
687 <https://doi.org/10.1038/ngeo1148>, 2011.

688 .

689

## 690 Figures and Tables

691



692

693 **Figure 1. Dissolved iron is strongly correlated with L<sub>1</sub> iron-binding ligands in diverse hydrothermal**

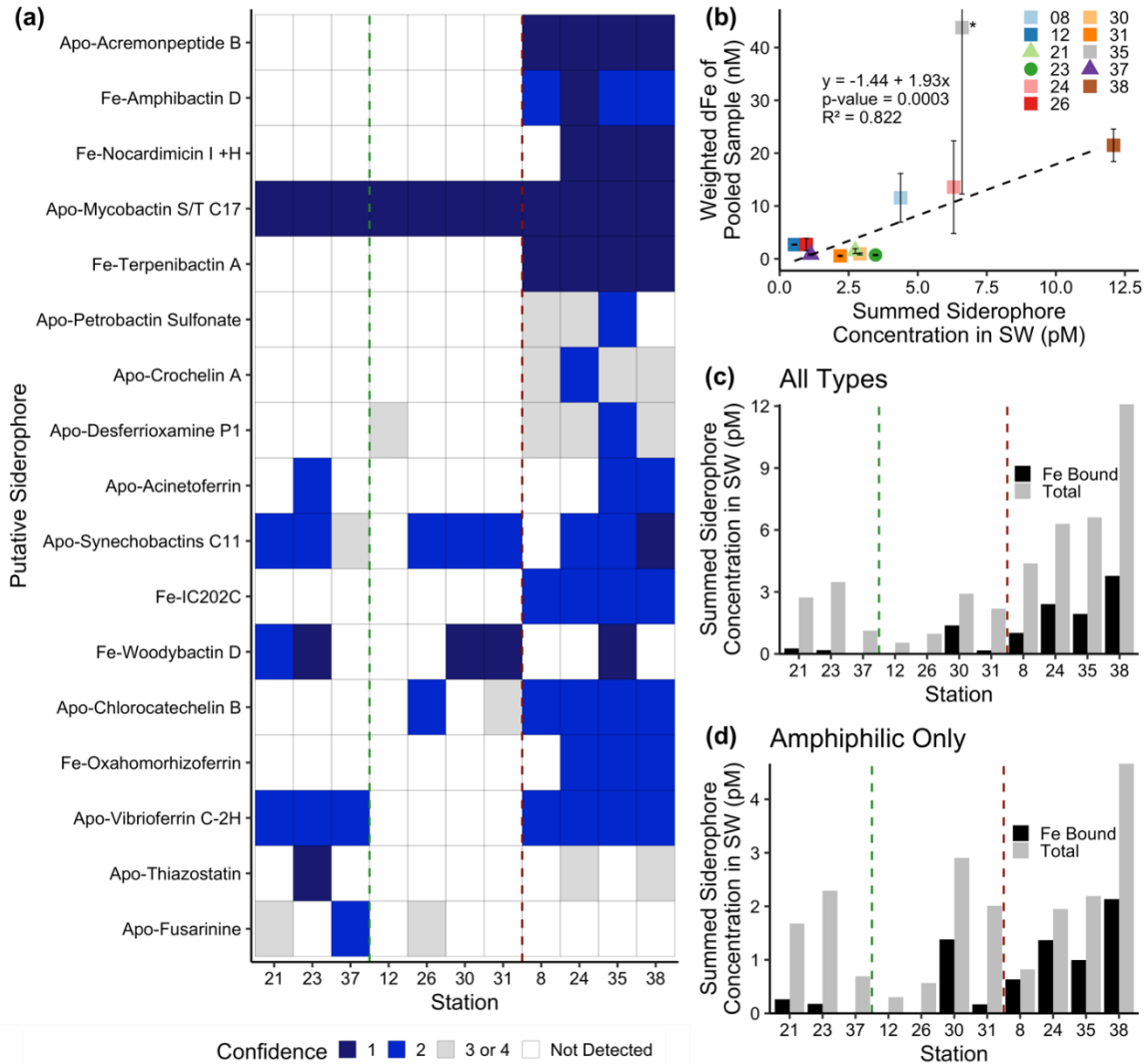
694 **systems.** (a) Station map showing the 11 sites investigated along the MAR. Known hydrothermal vents are

695 marked as red triangles (Beaulieu and Szafranski, 2020). Two expanded inset maps for (b) Rainbow and (c)

696 TAG hydrothermal vent fields. For additional information about vent site characteristics refer to **Table 1**. (d)  
697 dFe versus L<sub>1</sub> iron-binding ligands at each vent site in this study showing a ~1:1 correlation (m= 0.88, R<sup>2</sup>=  
698 0.96) with dFe in neutrally-buoyant plumes along the MAR. (e) dFe versus L<sub>1</sub> ligands from previous studies  
699 over the ridge axis and ~80 km from ridge axis in the Southern East Pacific Rise hydrothermal plume(Buck  
700 et al., 2018), and over TAG hydrothermal vent field(Buck et al., 2015). The solid black lines in (d) and (e)  
701 are the 1:1 ratio line between dFe and ligand concentrations, and dashed lines show the linear regression for  
702 the corresponding data. Square symbols refer to spreading centers, triangles refer to fracture zones, and  
703 circles refer to alkaline vents. Error bars represent the 95% confidence interval of the data fit as calculated  
704 by ProMCC(Omanović et al., 2015). The map was created using GeoMapApp version 3.6.14.

705

706

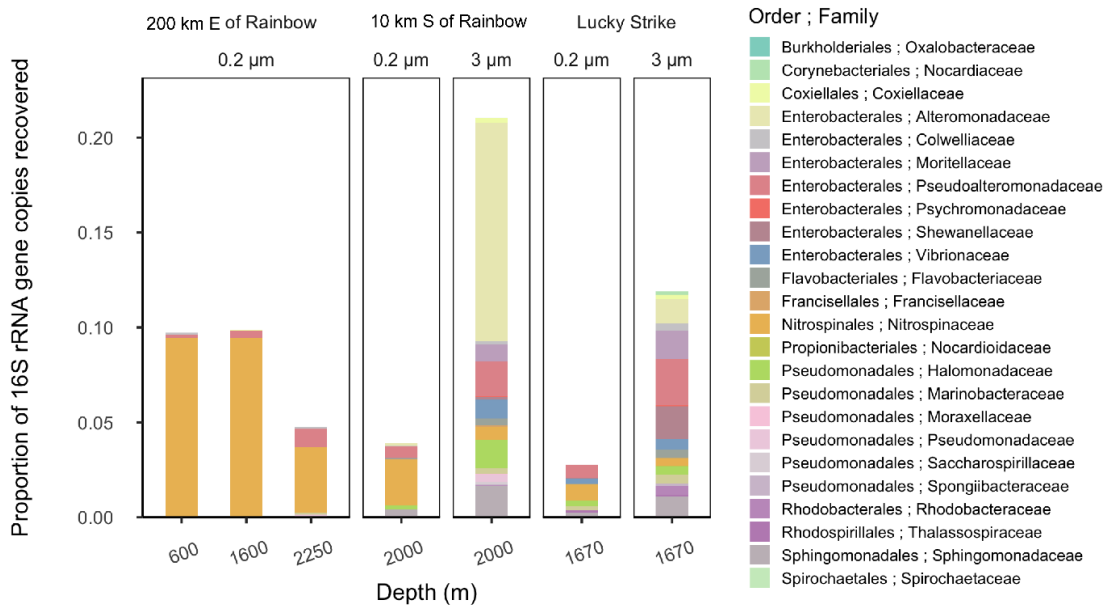


707

708

709 **Figure 2. Siderophore presence in hydrothermal plumes along the MAR.** (a) Heat map of confidence  
 710 levels 1-2 (blue gradient, 1 = highest confidence). Gray boxes indicate a detection with lower confidence (see  
 711 Methods), and white boxes indicate no detection at those sites. The y-axis is ordered from top to bottom in  
 712 terms of descending mass of the apo (without Fe) form of the siderophore. (b) Model II ordinary least squares  
 713 regression on dFe versus summed siderophore concentrations (of detections in Fig. 2b), calculated from peak  
 714 areas, at each site. Since the siderophore analysis was performed on pooled samples, the dFe values in the  
 715 regression are weighted values based on measured dFe and volume of each constituent of the pooled sample.  
 716 The vertical error bars represent the standard deviation of dFe of the constituents. TAG (St. 35) — denoted  
 717 by the asterisk — was not included in the regression due to its large range of dFe values and outlier behavior.  
 718 (c-d) Fe bound versus total summed concentration of (c) all types of siderophores and (d) amphiphilic  
 719 siderophores at each station. The vertical green lines separate fracture/diffuse sites from off-axis sites and  
 720 vertical red lines separate off-axis from on-axis sites as defined in Table 1. Symbols follow Fig. 1.

721



722

723

724 **Figure 3. Relative abundance of putative siderophore-producing taxa.** Bar height indicates the proportion  
 725 of 16S rRNA genes recovered in each sample, separated by depth from water surface, filter size fraction, and  
 726 site location. Colors correspond to taxonomy. Genera found in MAR vent microbial communities with  
 727 members in the antimash database predicted to produce siderophores are depicted at the family level.

728

**Table 1. Characteristics of sample locations along the Mid Atlantic Ridge.**

Vent Names	Abbr.	Station	Geology	Host rock	Vent type	Spreading rate (mm/yr)	Summed putative siderophore concentration (pM)	Summed Siderophore concentration/ L <sub>1</sub> ligand (%)*
Lucky Strike	LS	7/8	Spreading Center	gabbro	Black smoker	20.2	4.38	0.034-0.19
33 km E of Rainbow	CER	12	Spreading Center	-	-	-	0.537	0.013-0.017
Rainbow	R	38	Spreading Center	ultramafic	Black smoker	20.6	12.1	<i>n.a.</i>
Hayes Fracture Zone	HFZ	21	Fracture Zone	peridotites/gabbro	-	21.2	2.74	0.20-0.39
Lost City	LC	23	Fracture Zone	ultramafic/gabbro	Alkaline	22.6	3.47	0.27-0.35
Broken Spur	BS	24	Spreading Center	gabbro	Black smoker/diffuse	22.9	6.30	0.07-0.29
29 km N of TAG	CNT	26	Spreading Center	-	-	-	0.968	0.014-0.079
30 km W of TAG	CWT	30	Spreading Center	-	-	-	2.91	0.15
30 km E of TAG	CET	31	Spreading Center	-	-	-	2.19	0.31

Trans-Atlantic Geotraverse	TAG	35	Spreading Center	gabbro	Black smoker	23.6	6.61	0.18
Low Temp Slope	LTS	37	-	-	Diffuse fluids	-	1.13	0.079-0.087

Spreading rates along the Mid-Atlantic Ridge were gathered from the Interridge Database v3.4. Host rock groups were determined from previously discussed classifications (Bazylev, 1997; Kelley and Shank, 2010). Off-axis sites –33 km E of Rainbow, 29 km N of TAG, 30 km E of TAG, and 30 km W of TAG– were far-field locations of their respective vent field. Low Temp Slope was a diffuse-dominated site that was sampled for the first time as a part of this study. Summed putative siderophore concentrations and the percent of L<sub>1</sub> ligand are reported for compounds detected with at least confidence level 1 and 2 at one site. These values do not take into account typical extraction efficiencies of ENV columns for Fe-binding organics. Average L<sub>1</sub> ligand and siderophore concentrations can be viewed in **Table S3** and concentrations for individual siderophores can be observed in **Table S5**.

\*The siderophore sample at each site was pooled from ligand samples, so the percentage of siderophores in the L<sub>1</sub> pool is presented as a range based on the range of L<sub>1</sub> concentrations at each site.

*n.a.* = unable to be determined

- = unknown



